applied optics

Seasonal bias in global ocean color observations

K. M. Bisson,[1,*] ⓘ **E. Boss,**[2] ⓘ **P. J. Werdell,**[3] **A. Ibrahim,**[3] ⓘ **R. Frouin,**[4] AND
M. J. Behrenfeld[1]

[1]*Department of Botany and Plant Pathology, Oregon State University, Corvallis, Oregon 97331, USA*
[2]*School of Marine Sciences, University of Maine, Orono, Maine 04469, USA*
[3]*Ocean Ecology Laboratory, NASA Goddard Space Flight Center, Greenbelt, Maryland 20771, USA*
[4]*Scripps Institution of Oceanography, La Jolla, California 92093, USA*
Corresponding author: bissonk@oregonstate.edu

In this study, we identify a seasonal bias in the ocean color satellite-derived remote sensing reflectances ($R_{rs}(\lambda)$; sr^{-1}) at the ocean color validation site, Marine Optical BuoY. The seasonal bias in $R_{rs}(\lambda)$ is present to varying degrees in all ocean color satellites examined, including the Visible Infrared Imaging Radiometer Suite, Sea-Viewing Wide Field-of-View Sensor, and Moderate Resolution Imaging Spectrometer. The relative bias in R_{rs} has spectral dependence. Products derived from $R_{rs}(\lambda)$ are affected by the bias to varying degrees, with particulate backscattering varying up to 50% over a year, chlorophyll varying up to 25% over a year, and absorption from phytoplankton or dissolved material varying by up to 15%. The propagation of $R_{rs}(\lambda)$ bias into derived products is broadly confirmed on regional and global scales using Argo floats and data from the cloud-aerosol lidar with orthogonal polarization instrument aboard the cloud-aerosol lidar and infrared pathfinder satellite. The artifactual seasonality in ocean color is prominent in areas of low biomass (i.e., subtropical gyres) and is not easily discerned in areas of high biomass. While we have eliminated several candidates that could cause the biases in $R_{rs}(\lambda)$, there are still outstanding questions regarding potential contributions from atmospheric corrections. Specifically, we provide evidence that the aquatic bidirectional reflectance distribution function may in part cause the observed seasonal bias, but this does not preclude an additional effect of the aerosol estimation. Our investigation highlights the contributions that atmospheric correction schemes can make in introducing biases in $R_{rs}(\lambda)$, and we recommend more simulations to discern these influence $R_{rs}(\lambda)$ biases. Community efforts are needed to find the root cause of the seasonal bias because all past, present, and future data are, or will be, affected until a solution is implemented.   © 2021 Optical Society of America

1. INTRODUCTION

Spectral remote sensing reflectances ($R_{rs}(\lambda)$; sr^{-1}) are the fundamental measurements that link the marine environment to ocean color satellite observations. Since the launch of the coastal zone color scanner in 1978, satellite observations of $R_{rs}(\lambda)$ have been used to derive biogeochemical variables (e.g., chlorophyll ([chl], mg m^{-3}), spectral particulate backscattering ($b_{bp}(\lambda)$, m^{-1}), spectral particulate absorption ($a_p(\lambda)$m^{-1}), spectral phytoplankton absorption ($a_{ph}(\lambda)$, m^{-1}), and spectral dissolved organic matter absorption [$a_{dg}(\lambda)$m^{-1}]). These products have subsequently been used to quantify global net primary production [1,2], global carbon export and associated pathways for sinking (e.g., [3]), particulate organic carbon stocks [4,5], suspended particle sizes [6,7], metrics of phytoplankton community composition [8–12], harmful algal blooms [13–15], phytoplankton carbon and physiology [16,17], nitrogen fixation [18], river plumes and suspended sediment concentrations [19–21], dissolved organic matter concentrations [22,23],

metrics of general ecological dynamics [24], and references therein, and metrics associated with climate change [25–27].

Accurate, low-uncertainty, and unbiased satellite $R_{rs}(\lambda)$ observations are critical for advancing our understanding of the marine carbon cycle and improving the predictive power of ecological and climate models. New technologies have allowed evaluation of ocean color R_{rs}-derived products on global scales, particularly Argo and satellite lidar measurements [28–31]. Recently we compared $b_{bp}(\lambda)$ derived from moderate resolution imaging spectrometer onboard Aqua (MODIS-Aqua) $R_{rs}(\lambda)$ with both $b_{bp}(532)$ from the cloud-aerosol lidar with orthogonal polarization (CALIOP) instrument aboard the coud-aerosol lidar and infrared pathfinder (CALIPSO) satellite and $b_{bp}(531)$ measured on Argo floats. We found that the two satellite sensors retrieved b_{bp} with relative errors $< 30\%$ and that CALIOP data were more consistent with float estimates of $b_{bp}(531)$ than MODIS -Aqua. The ratio of MODIS-Aqua-to-CALIOP b_{bp} revealed global differences that in some regions exceeded 50%

[29], motivating the current examination of the basis for these differences.

We approached our analysis agnostically, assuming that either or both MODIS-Aqua or CALIOP could be spatiotemporally biased. On one hand, CALIOP b_{bp} is sensitive to the scattering phase function, which can vary both seasonally and spatially depending on in-water particle characteristics. On the other hand, MODIS-Aqua b_{bp} is retrieved from $R_{rs}(\lambda)$ based on assumptions regarding absorption and scattering contributions of in-water constituents. In addition, MODIS-Aqua $R_{rs}(\lambda)$ retrievals involve an atmospheric correction, requiring inferences on atmospheric aerosol contributions to total observed signal [32]. Spatiotemporal differences in b_{bp} between satellite sensors may also arise from viewing angle differences [33], noting here that CALIOP is a nadir viewing sensor, while MODIS-Aqua operates at viewing angles ± 49.5 deg relative to nadir.

Given the above considerations, we used $R_{rs}(\lambda)$ data from the Marine Optical BuoY (MOBY) site as the central basis for evaluating MODIS-Aqua and CALIOP b_{bp} differences. MOBY is a long-duration moored radiometer system located off the coast of Lanai, Hawaii, and its time-series data are considered the "gold standard" for calibration and validation of satellite ocean retrievals [34]. We find that the seasonal cycle in CALIOP b_{bp} is consistent with MOBY data, whereas a seasonal bias is evident in ocean color-based b_{bp}. This ocean color bias is found across sensors [MODIS-Aqua, sea-viewing wide field of view sensor (SeaWiFS), visible infrared imagining radiometer suite (VIIRS)], and we provide preliminary evidence that it arises from the applied bidirectional reflectance distribution function (BRDF) and other residual effects of the ocean color atmospheric correction. At the time of this writing, no solution has been established to correct the seasonal mismatch between ocean color data and MOBY. We call for additional community assistance with this issue, as its resolution is fundamental to our understanding of aquatic ecology and for ensuring success of future satellite missions, such as plankton, aerosol, cloud, ocean ecosystem (PACE) [35].

2. METHODS

This section describes our evaluation of MODIS-Aqua, VIIRS, SeaWiFS, and CALIOP data at the MOBY site. We also describe global CALIOP b_{bp} (532) and regional Argo b_{bp} (700) data used to globally extend our primary findings at the MOBY site.

A. Satellite Ocean Color and MOBY R_{rs}

We retrieved MODIS-Aqua, SeaWiFS, and VIIRS Level-2 satellite $R_{rs}(\lambda)$ paired with $R_{rs}(\lambda)$ measured at the MOBY site using the NASA Ocean Biology Processing Group (OBPG) validation tool [36], which provides paired MOBY measurements and unflagged, same-day satellite observations following the [37,38] criteria (specifically, at least half of the satellite pixels in a 5×5 box around the *in situ* observation must be unflagged and the paired observations must be within 3 h of each other). We calculated (from match-up pairs) monthly averages of MOBY and MODIS-Aqua $R_{rs}(\lambda)$ at 412, 443, 488, 547, and 667 nm (n = 523, with < 5 0 observations in

the March–October averages). We calculated MOBY and MODIS-Aqua chlorophyll concentration ([chl], mg m^{-3}) using the standard band-ratio algorithm ("OC3m") [39]. We also ran the gneralized inherent optical properties algorithm in default configuration (GIOP-DC)) [40] on MOBY and MODIS-Aqua $R_{rs}(\lambda)$ data to produce $b_{bp}(\lambda)$, phytoplankton absorption ($a_{ph}(\lambda)$), and absorption by colored material and nonalgal particles ($a_{dg}(\lambda)$). Monthly VIIRS $R_{rs}(\lambda)$ averages were calculated at 410, 443,486, 551, and 671 nm ($n = 232$, with < 10 observations in April, July, and September). SeaWiFS (λ) monthly R_{rs} averages were calculated at 412, 443,490, 510, 555, and 670 nm ($n = 769$, with < 50 observations for May, June, and July). Standard errors for all $R_{rs}(\lambda)$ observations were calculated from the standard deviation and number of monthly observations.

Using exact matchups between MOBY and satellite sensors limits the amount of data used in evaluating ocean color. Therefore, we also downloaded all available MODIS-Aqua and MOBY data at the MOBY site (from the OBPG time series tool [41]) to confirm that the seasonal mismatches exist when all data are used to quantify the seasonal cycles of MODIS-Aqua and MOBY $R_{rs}(\lambda)$ (Supplement 1 Fig. 4). The time series tool provides ocean color data at a larger spatial range than the 5×5 pixel box used in the validation tool (Supplement 1).

B. CALIOP at MOBY

CALIOP is a light detection and ranging (lidar) instrument flying in the A-train constellation with MODIS-Aqua and intended for cloud and aerosol retrievals. Nevertheless, repeated global sampling of subsurface ocean b_{bp} (532) has been achieved with CALIOP using its polarization channels (see details in [42]), providing an independent assessment of b_{bp} for comparison with MODIS-Aqua (see Supplement 1 of [29]). We acquired daily CALIOP b_{bp} (532) data from 2006 to 2017 from the Oregon State University Ocean Productivity website [43] and used daytime data under both cloudy and clear conditions. A scattering phase function (at an angle of π) of 0.32 was used to calculate CALIOP b_{bp} (532), following [29,44,45]. All CALIOP daily data (with a 90 m footprint) were binned into monthly 1-deg grids for each year of data. These monthly values were then averaged to form monthly climatologies at the MOBY site (note that MODIS-Aqua data are restricted to the same time period when compared to CALIOP observations).

C. Ancillary Data: Regional and Global b_{bp} Products

Few ocean color validation sites like MOBY exist worldwide. We therefore used Argo and CALIOP data to more broadly examine the ocean color $R_{rs}(\lambda)$ biases established at the MOBY site. Argo floats provide independent *in situ* measurements of b_{bp}(700) worldwide that are useful for comparison with satellite data. Vertical profiles of b_{bp}(700) were downloaded from the Argo Data Assembly Centre and processed as in [28]. The vertical profiles were despiked with a 3-pt moving median and the median b_{bp}(700) value calculated for the mixed layer (defined as the depth were density exceeded the 10 m value by 0.03 kg^{-3}). We extrapolated Argo b_{bp}(700) to b_{bp}(531) for comparison with MODIS-Aqua (and CALIOP's b_{bp}(532))

using the backscattering slope (γ, unitless) derived within GIOP-DC from colocated MODIS-Aqua $R_{rs}(\lambda)$ (see Eq. (2) in Supplement 1). Previous work compared point-by-point matchups between Argo, MODIS-Aqua, and CALIOP and found that CALIOP outperformed MODIS-Aqua with respect to $b_{bp}(531)$ retrievals (where median percent errors were 25% for MODIS-Aqua and 16% for CALIOP, relative to an uncertainty of <15% for Argo backscattering sensors [29]). Here, we instead compare seasonal cycles of Argo, MODIS-Aqua, and CALIOP b_{bp}. Because there are insufficient measurements of Argo $b_{bp}(531)$ for any given month, we calculated monthly averages over the entirety of Argo sampling period for specific regions. For the global comparison of CALIOP b_{bp} (532) and MODIS-Aqua b_{bp} (531), daily CALIOP and Level-3 MODIS-Aqua b_{bp} data were binned into 1-deg composites and then monthly climatologies constructed for the shared time period of 2006-2017 (see Supplement 1 for additional information on MODIS-Aqua b_{bp} processing).

D. Multivariate Regression Analysis on MOBY and MODIS Data

Multivariate regression (MLR) analysis provides insight into the dependence of the $R_{rs}(\lambda)$ matchups on other matchup variables that are considered in the atmospheric correction. The atmospheric correction process removes radiometric contributions of atmospheric gases, aerosols, surface glint, and whitecaps from the observed top-of-atmosphere signal. The correction also applies a BRDF adjustment to ultimately derive a final $R_{rs}(\lambda)$ [32]. We utilized a probabilistic programming Python library, PyMC3, for the MLR, allowing us to estimate the posterior distribution of regression coefficients from explanatory variables given a prior probability [46]. Using the MLR analysis, we modeled MODIS-Aqua $R_{rs}(\lambda)$ (Rrs$_{aqua}$, derived from satellite data after the atmospheric correction) as a function of all other variables, including MOBY $R_{rs}(\lambda)$ (Rrs$_{moby}$), the BRDF correction factor ($f_{brdf}(\lambda)$), wind speed (W_s), Sun glint contribution (L_{GN}), column water vapor (Cwv), column ozone (O_3), pressure (Pr), relative humidity (Rh), Ångström coefficient (α_a), aerosol optical depth (τ_a), and the solar zenith (θ_{sol}), sensor zenith (θ_{sen}), and relative azimuth (φ) angles. The regression model is assumed to follow a Student's t distribution, rather than a normal distribution, because Student's t allows for additional degrees of freedom to compensate for strong outliers (i.e., allows for a more robust linear regression). This assumption is, in effect, similar to the outliers filtering procedure used in the vicarious calibration process at MOBY, as it excludes points outside the interquantile range [47]. Rrs$_{aqua}$ is modeled as follows:

$$R\mathrm{rs}_{aqua} \sim \mathrm{St}\,(\mu,\ \nu), \tag{1}$$

where μ and ν are the mean and degree of freedom of the Student's t distribution, respectively, and μ is modeled as

$$\mu = \beta_0 \mathrm{Rrs}_{moby} + \beta_1\theta_{sol} + \beta_2\theta_{sen} + \beta_3\varphi + \beta_4 W_s + \beta_5 L_{GN}$$

$$+ \beta_6 Cwv + \beta_7 Rh + \beta_8 O_3 + \beta_9 Pr + \beta_{10}\alpha_a + \beta_{11}\tau_a$$

$$+ \beta_{12} f_{brdf} + \alpha. \tag{2}$$

Slope coefficients of each variable Eq. (2) are denoted as β_i and α is the intercept. The prior distribution of β_i and α are assumed weakly informative, with mean of zero and a standard deviation of 100. Since the magnitude and dynamic range of each variable is different, we scaled the data by subtracting the mean and dividing by the standard deviation of each variable (thus, all data have a mean of zero and a standard deviation of one). The intercept bias (α) is thus zero. In this manner, the magnitude of the slopes become more meaningful, such that one unit of change of the dependent variable is equivalent to one unit of change of the independent variables when a specific β_i is 1 (indicating a one-to-one correspondence between the two variables).

3. RESULTS

Relative to MOBY $R_{rs}(\lambda)$, seasonal cycles of ocean color $R_{rs}(\lambda)$ are pronounced, with higher $R_{rs}(\lambda)$ in spring and summer and lower values in fall and winter (Figs. 1 and 2).

A. Seasonal Bias in Ocean Color $R_{rs}(\lambda)$ at MOBY

MOBY $R_{rs}(\lambda)$ data are primarily used for system-level vicarious calibration of ocean color satellites [48]. Therefore, it is reasonable to expect that the average seasonal magnitudes of satellite-derived $R_{rs}(\lambda)$ should mimic those from MOBY (noting that system vicarious calibration adjusts average absolute instrument plus atmospheric correction differences, not short-term (e.g., seasonal) instrument temporal drift). Monthly averaged $R_{rs}(\lambda)$ at various wavelengths between ocean color satellite observations and MOBY exhibit discrepancies over the seasonal cycle (Figs. 1 and 2). At shorter wavelengths (412 and 443 nm), discrepancies between MOBY (red line) and either MODIS-Aqua [Figs. 1(a)–1(e)], VIIRS [Figs. 1(f)–1(j)], or SeaWiFS [Figs. 1(k)–1(o), black lines] are minimal [Figs. 1(a) and 1(b)], and the general seasonal cycle is consistent between data sets. However, at longer wavelengths (486–671 nm, where the effect of Raman scattering is important), the seasonal cycle of ocean color $R_{rs}(\lambda)$ is very different from that of MOBY. MOBY exhibits little to no seasonality for wavelengths exceeding 500 nm. In contrast, monthly averages of ocean color $R_{rs}(\lambda) > 500$ nm tend to be elevated in summer compared to other seasons. Overall, MODIS-Aqua and VIIRS tend to exhibit higher magnitudes of a seasonal bias compared to SeaWiFS.

Discrepancies in $R_{rs}(\lambda)$ seasonal cycles exist among the three ocean color satellite sensors, perhaps in part reflecting different sample sizes per month (i.e., due to sampling bias, varied viewing and solar geometries at the time of observation, or both). Correlations across the same wavelengths of different sensors are generally good (R $\sim$ 0.8), except in the red (where R $\sim$ 0.4). Additionally, two sample t-tests to determine statistical differences (which explicitly incorporate sample size and variance for each month) generally show similarity across sensor comparisons (by wavelength and month), although $\sim$30% of instances reveal statistically significant differences that may reflect inadequate sampling. Future and ongoing work should incorporate greater uncertainty analyses, as well as simulations, to determine the degree to which the three sensors differ.
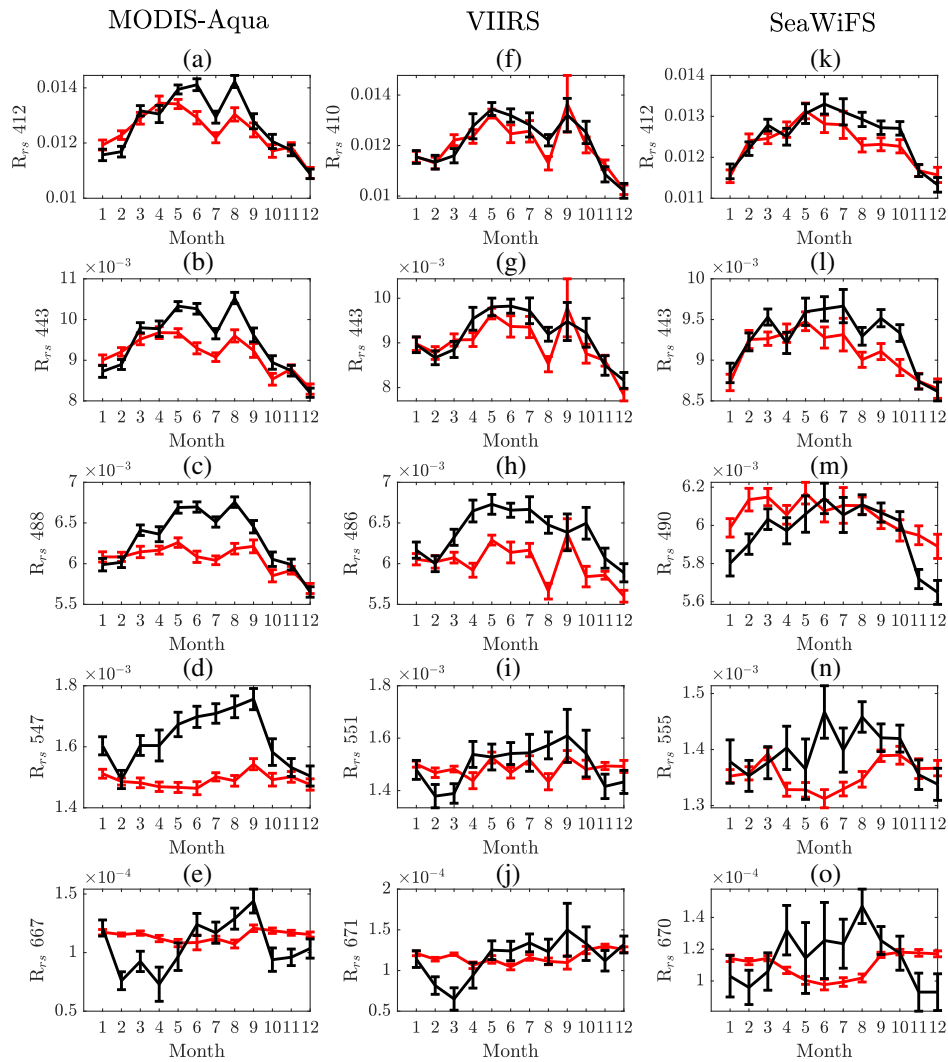
Fig. 1.   Monthly averaged $R_{rs}(\lambda)$ with standard error bars for paired validation observations between (a)–(e) MODIS-Aqua, black line; (f)–(j) VIIRS, black line; (k)–(o) SeaWiFS, black line, and MOBY (red line), for each month. Note that wavelengths displayed in a row are not always similar.

The shape of the ocean color $R_{rs}(\lambda)$ seasonal cycle at MOBY also varies slightly different between satellite sensors (compare red lines in Fig. 1). When all MOBY data are used (Supplement 1 Fig. 4), $R_{rs}(\lambda)$ exhibits a seasonality with relatively higher values in the summer for the longer wavelengths. In general, these patterns are preserved in the validation matchups shown in Fig. 1, but can be obscured by the *y* axes for each sensor (e.g., compare the last row, Fig. 1).

Relative differences between MODIS-Aqua [Figs. 2(a)–2(e)], VIIRS [Figs. 2(f)–2(j)], SeaWiFS [Figs. 2(k)–2(o)], and MOBY are relatively modest (on the order of 10%) for $R_{rs}(\lambda)$ observations between 412 and 555 nm, but at 667 nm and 671 nm the differences can reach 50% (noting, however, that the absolute signal at these red wavelengths is much lower than the blue bands). The biggest discrepancies between satellite ocean color and MOBY $R_{rs}(\lambda)$ are during the summer months for all wavelengths. These months also have the most sparse and constrained geometric sampling due to the exclusion of Sun-glint contaminated data. When all data are used to compile monthly

averages, rather than restricting data to validation matchups, relative biases range from 20%-40% (see Supplement 1 Fig. 4).

B. Biases in $R_{rs}(\lambda)$-Derived Products at MOBY

When MOBY and MODIS-Aqua $R_{rs}(\lambda)$ are used to derive $b_{bp}(\lambda)$, the seasonal cycle observed between the two sensors is markedly different (Fig. 3). MOBY $b_{bp}(531)$ (black dotted line) and CALIOP $b_{bp}(532)$ (blue solid line) exhibit weak seasonality at this location compared to MODIS − Aqua $b_{bp}(531)$ [red line, Fig. 4(a)]. The MODIS-Aqua $b_{bp}(531)$: MOBY $b_{bp}(531)$ and MODIS-Aqua $b_{bp}(531)$: CALIOP $b_{bp}(532)$ ratios have the same general shape over the annual cycle, again suggesting that MOBY and CALIOP retrievals are more similar to each other than either is to MODIS-Aqua [Fig. 3(b)]. The seasonal bias between MODIS-Aqua and CALIOP backscattering (black solid line) is ∼10% different compared to ∼30% different between MODIS-Aqua and MOBY (black dotted line) for the peak $b_{bp}(531)$ difference between sensors (which
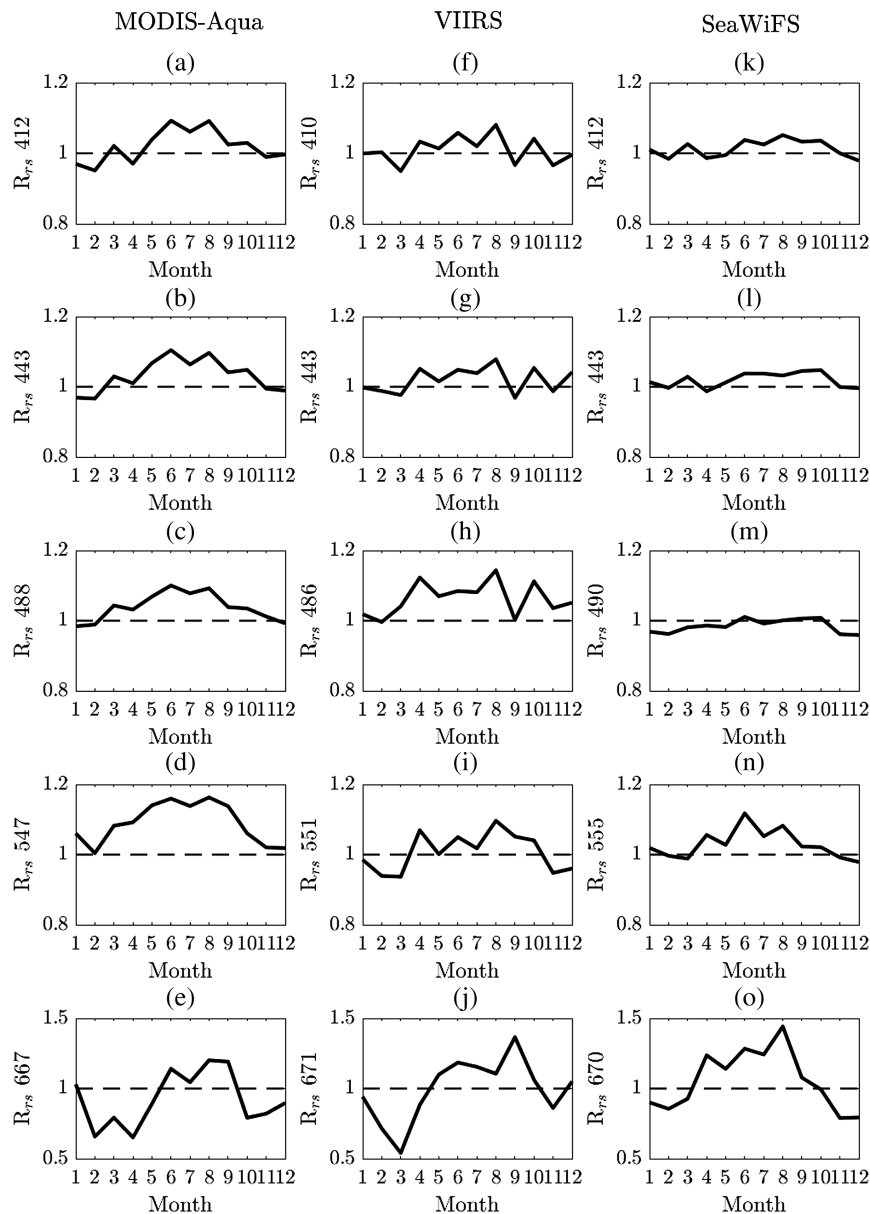
Fig. 2. Ratios of ocean color R_{rs} to MOBY R_{rs} for (a)–(e) MODIS-Aqua; (f)–(j) VIIRS; and (k)–(o) SeaWiFS. Average monthly values for each satellite sensor are compared with average MOBY validation data over a shared time period where data are available.

occurs around May to August). These differences are largely because CALIOP $b_{bp}(532)$ exceeds MOBY $b_{bp}(531)$ (Fig. 3(b), [29]). Overall, the observed seasonal bias between MODIS-Aqua and MOBY at this local site is consistent with the seasonal bias between MODIS-Aqua and CALIOP on global scales. MODIS-Aqua $b_{bp}(531)$ greatly exceeds MOBY $b_{bp}(531)$ during the summer months compared to the winter months in the northern hemisphere.

In addition to $b_{bp}(\lambda)$, we also used MOBY and MODIS-Aqua $R_{rs}(\lambda)$ data to calculate phytoplankton absorption [$a_{ph}(443)$, red line in Fig. 3(c)], absorption from dissolved detrital organic matter plus nonalgal particles [$a_{dg}(412)$, blue line in Fig. 3(c)], and chlorophyll ([chl], green dashed line in Fig. 3(c)). In contrast to MOBY and MODIS-Aqua $b_{bp}(531)$, all of the absorbing constituents derived from MODIS-Aqua

$R_{rs}(\lambda)$ are lower on average compared to MOBY, although the differences are smaller than that for $b_{bp}(531)$. Differences in [chl] for MOBY and MODIS-Aqua can reach 20% from March to April, while differences for $a_{dg}(412)$ and $a_{ph}(443)$ remain below 15% throughout the annual cycle.

C. MLR Analysis Findings

Results from the MLR analysis (Fig. 4) indicate a significant dependence of Rrs_{aqua} on the solar and sensor zenith angle at almost all wavelengths, as well as on BRDF slope (β) across wavelengths. A β close to 0 indicates no correspondence with Rrs_{aqua}, while a negative β indicates an inverse relationship. Ideally, the β_0, slope between Rrs_{aqua} and Rrs_{moby} should be 1, while the slope for other independent variables should
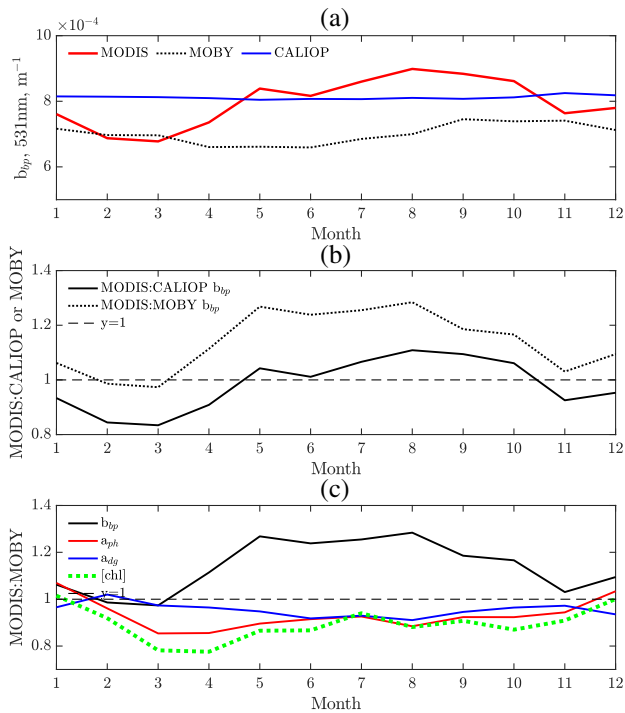
Fig. 3. Comparison of MODIS-Aqua $b_{bp}(531)$ with CALIOP $b_{bp}(532)$ and MOBY retrievals at the MOBY site. (a) Monthly averaged MODIS-Aqua (red), MOBY (black dashed line), and CALIOP (blue) $b_{bp}(\lambda)$; (b) MODIS-Aqua $b_{bp}(531)$: CALIOP $b_{bp}(531)$ (black solid line) and MODIS-Aqua $b_{bp}(531)$: MOBY $b_{bp}(531)$ (black dotted line). Dashed line indicates a ratio of 1. (c) MODIS-Aqua:MOBY $b_{bp}(531)$, MODIS-Aqua:MOBY $a_{ph}(443)$ (red line), MODIS-Aqua: MOBY $a_{dg}(412)$ (blue line), MODIS-Aqua:MOBY chlorophyll (green dashed line, calculated using the standard band-ratio "OC3m" algorithm). All averages are calculated within a shared time period of 2006–2017.

be 0 (indicating independence between the variables and the $R_{rs}(\lambda)$ matchups). A deviation in β from 0 indicates a residual bias in the matchups due to improper correction to

these parameters on their relationship with Rrs_{aqua}. The slope coefficient for Rrs_{moby} approaches 0 at wavelengths 531 nm and greater.

At longer wavelengths, slopes for the optical depth and the Ångström coefficient deviate from 0, as well as the slope for the glint contribution (particularly at 667 and 678 nm). At wavelengths 412 and 443 nm, other than the zenith angles, the BRDF correction factor has the largest s, indicating that this correction has the most colinearity with the $R_{rs}(\lambda)$ matchups. The BRDF slope decreases for longer wavelengths, and the slope of the Ångström coefficient and the optical depth is more pronounced. Overall, the BRDF slope showed a consistent and statistically significant departure from the zero line at all wavelengths. However, the aerosol correction also plays a role.

D. Confirmation of a Bias in Ocean Color Products at Regional and Global Scales

To learn if a seasonal bias exists in ocean color products at larger scales beyond MOBY (and also to test if the general results at MOBY are site-specific), we compared MODIS-Aqua and CALIOP data with *in situ* b_{bp} from Argo floats in the South Pacific, Indian Ocean, and South Atlantic (Supplement 1 Figs. 1–3). These comparisons reveal that the seasonal cycle of MODIS-Aqua is unlike the seasonal cycle of either CALIOP or Argo. In particular, MODIS-Aqua b_{bp} is symmetric across the annual cycle and has more pronounced seasonality compared to CALIOP or Argo. Thus, the pattern in ocean color seasonality observed at the MOBY site appears to also broadly exist in MODIS-Aqua $b_{bp}(531)$ data at global scales (Supplement 1 Fig. 5, Visualization 1, Visualization 2, Visualization 3, Visualization 4, Visualization 5, Visualization 6, Visualization 7, Visualization 8, Visualization 9, Visualization 10).

On a region-to-region basis, seasonal patterns in MODIS-Aqua data show both similarities and differences with the CALIOP and Argo data (Fig. 5). For example, in the North Atlantic and Arctic, the seasonal cycles of MODIS-Aqua, Argo, and CALIOP agree well. In contrast, the magnitude of
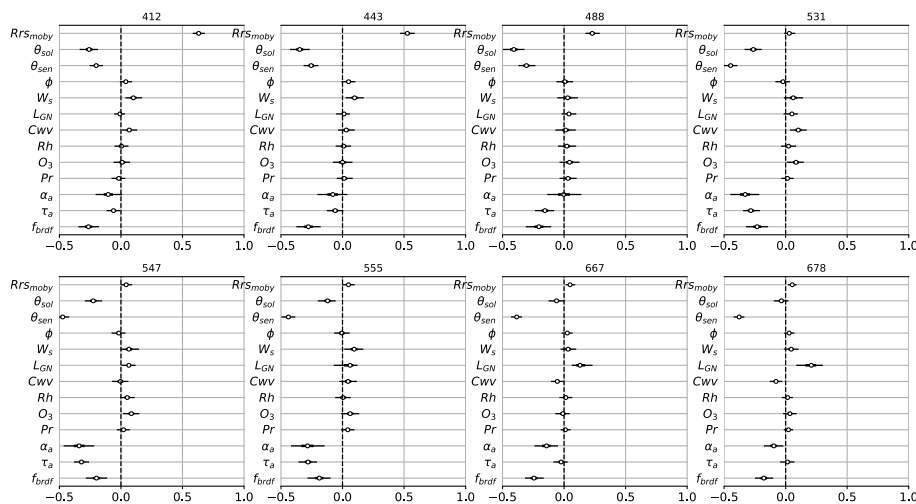

Fig. 4. Forest plot of the MLR slope coefficients for wavelengths 412, 443, 488, 531, 547, 555, 667, and 678 nm. The y axis shows the β coefficients for each explanatory variable and the x axis shows the scale of these coefficients. The open circle represents the mode of the posterior, while the error bar represents the 94% high density interval of the distribution.
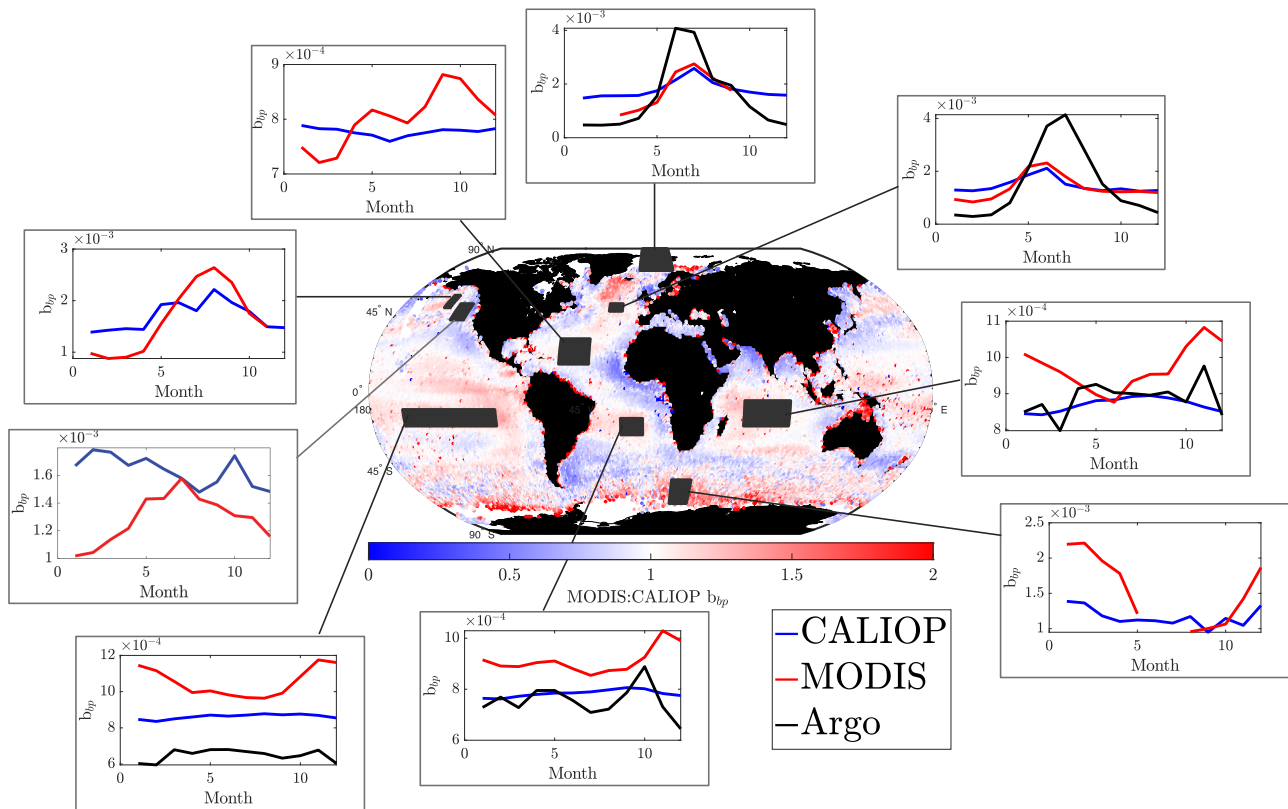
Fig. 5. Global comparisons of MODIS-Aqua $b_{bp}(531)$ and CALIOP $b_{bp}(532)$. The ratio of annually averaged MODIS-Aqua to annually averaged CALIOP b_{bp} is mapped. Both MODIS-Aqua and daytime CALIOP data were binned to 1 deg and averaged over a shared time period of 2006–2017 to form monthly averages. When Argo data are available (with at least 200 independent observations over the annual cycle) monthly averages of Argo b_{bp} (531) are plotted (black) alongside MODIS-Aqua (red) and CALIOP (blue) b_{bp}.

MODIS-Aqua b_{bp} and its seasonal cycle disagree with both Argo and CALIOP data in low-biomass regions (e.g., South Pacific, South Atlantic, Indian Ocean) (Fig. 5) (one exception, here, is the South Atlantic, where the shape of the seasonal cycle in MODIS-Aqua b_{bp} is better aligned with Argo data than CALIOP, but the magnitude of MODIS-Aqua data is ~30% higher than either CALIOP or Argo). The Indian Ocean, South Pacific, and northeast Pacific sites exhibit symmetrical (relative to the central month of June) seasonal cycles in MODIS-Aqua b_{bp}. In summary, the Argo and CALIOP data appear to confirm over a much broader scale the findings reported above for the MOBY site.

4. DISCUSSION

Here, we present significant seasonal mismatches between ocean color satellite data products and equivalent retrievals from other independent sources (MOBY, CALIOP, and Argo). In many cases, the mismatches in $R_{rs}(\lambda)$ observations are roughly symmetrical over the annual cycle, which is difficult to reconcile with known seasonal plankton cycles, which tend to be asymmetric with respect to the seasonal cycle (e.g., [49,50]). Seasonal symmetry is expected, however, if the source of the issue is linked to solar geometry (including day length, which is directly proportional to solar zenith angle). Therefore, the observed shape in $R_{rs}(\lambda)$ over the annual cycle strongly implies that the observed

seasonal biases are related not to in-water processes but artifacts stemming from data processing. Our analysis has eliminated many potential candidates causing the seasonal biases, but we have not yet identified the specific issue(s). Nevertheless, we can still examine the extent to which the bias is problematic for different regions and times. Here, we reflect on what is learned from cross-comparing observational platforms to discover the widespread seasonal bias in satellite ocean color observations.

A. Importance of Additional Assets to Improve Remote Sensing

Our discovery of the ocean color seasonal bias highlights the importance of multiple independent satellite and *in situ* data sets for performance evaluations (in addition to traditional coincident satellite-to-*in situ* match-ups). More specifically, CALIOP provided the first indications of a bias in ocean color products [29] and enabled a global extension of findings at the MOBY site. The high-quality time-series MOBY data were essential to "ground truth" the initial CALIOP finding and confirm that the bias is present in $R_{rs}(\lambda)$, not just products derived from $R_{rs}(\lambda)$. We also learn from MOBY that $b_{bp}(\lambda)$ retrievals are most strongly affected by the $R_{rs}(\lambda)$ biases in comparison to chlorophyll, phytoplankton absorption, and dissolved organic matter absorption retrievals. Finally, Argo data were vital for testing the accuracy of MODIS-Aqua and CALIOP products

at regional scales. Recognizing that a seasonal bias in ocean color products has existed but remained undetected for decades illustrates how the importance of independent data sets for evaluating remote-sensing products cannot be overstated.

Closure in $b_{bp}(\lambda)$ has not been reached between passive remote sensing, *in situ* sampling, and active remote sensing. In truth, none of these platforms fully measure $b_{bp}(\lambda)$, as the sensors employed observe scattering at different viewing angles and measure only part of the volume scattering function. CALIOP data do not exhibit the seasonal bias apparent in ocean color $R_{rs}(\lambda)$, which we speculate is due to the lidar making a more direct measurement of $b_{bp}(\lambda)$, being unaffected by Sun zenith angle, and having less sensitivity to atmospheric conditions (including clouds, e.g., [51] and references therein). In contrast, ocean color $R_{rs}(\lambda)$ is the remaining signal after removing estimated contributions of surface glint, whitecaps, and atmospheric molecules and aerosols, and following a BRDF correction. In addition, deriving $b_{bp}(\lambda)$ from $R_{rs}(\lambda)$ from ocean color requires spectral assumptions regarding scattering and absorbing constituents in seawater.

Satellite ocean color and lidar observations both exhibit an overall bias in b_{bp} for low-biomass areas. Argo $b_{bp}(531)$ observations in oligotrophic regions (South Pacific, South Atlantic, Indian ocean gyres) are roughly 30% lower than CALIOP $b_{bp}(532)$ and up to 50% lower than MODIS-Aqua $b_{bp}(531)$. These findings are consistent with our work [28], where we report a good correspondence between Argo, MODIS-Aqua, and CALIOP for b_{bp} values > 0.001 m^{-1}, but not for those < 0.001 m^{-1}. The reason for the elevated MODIS-Aqua and CALIOP retrievals in low-biomass regions is not yet understood, and continued work is needed to resolve this issue. The reason that the seasonal biases in ocean color are not as pronounced in high-biomass regions is likely because the ocean's biological signal is larger (relative to low-biomass regions) and less influenced by atmospheric corrections. Overall, the biases in ocean color retrievals yield seasonal patterns in many regions that are inaccurate and may be problematic, depending on the scale and intention of studies that use these measurements.

B. What Can We Learn about $R_{rs}(\lambda)$ from Diagnosing the Seasonal Bias?

In this study, we employed a series of diagnostic tests in an attempt to identify any underlying cause of the seasonal bias in satellite ocean color $b_{bp}(\lambda)$. Despite testing ideas thought to have a large influence on $b_{bp}(\lambda)$ (such as Raman correction, assumed spectral shape of absorption and backscattering), we found that specific assumptions in $R_{rs}(\lambda)$ inversions had little influence on the seasonal bias in $b_{bp}(\lambda)$. This finding implies that atmospheric correction schemes have a larger effect on R_{rs}-derived products than the current inversion models used to derive those products.

The larger relative bias in $R_{rs}(\lambda)$ for longer wavelengths appears to impact derived geophysical products that include longer wavelengths. For example, there is a clear seasonal bias in $b_{bp}(\lambda)$ derived from $R_{rs}(\lambda)$ at MOBY due to the inclusion of strongly biased $R_{rs}(531 - 667)$ into GIOP-DC. This clear $b_{bp}(\lambda)$ bias is present despite no pronounced seasonal bias for

shorter wavelengths included within the GIOP-DC inversion scheme.

All sensors in this study have uncertainty associated with their products, and MOBY is no exception. While the absolute laboratory calibrations of MOBY strictly adhere to National Institute of Standards and Technology (NIST)-traceable standards and processes [52], the final water-leaving signals require postprocessing and extrapolation from observations > 1 m depth. Errors in this extrapolation can approach 80% at longer wavelengths (e.g., see Fig. 7 of [53]). Since both MOBY and satellite data have relatively larger uncertainties in the green/red wavelengths, more realistic (wavelength-dependent) uncertainties should be included in future work [54].

C. Global Implications of R_{rs} Bias

Although the bulk of our analysis focused on the MODIS-Aqua sensor, the seasonal bias in satellite $R_{rs}(\lambda)$ is present in SeaWiFS and VIIRS imagery as well. The seasonal bias is larger in MODIS-Aqua and VIIRS compared to SeaWiFs, which may be a function of the different viewing angles between the sensors, as well as differences in local overpass times and solar geometries. Accurate seasonal measurements of $b_{bp}(\lambda)$ in particular are needed to characterize temporal dynamics of phytoplankton carbon [55] and particulate organic carbon. Phytoplankton carbon observations from satellites are used in many models, from net primary production to carbon export. Net primary production algorithms require growth rates calculated from phytoplankton physiological states, commonly assessed using satellite Chl:Carbon ratios [16]. Mechanistic carbon export models that use food-web interactions rely entirely on the derivative of phytoplankton carbon over the annual cycle in order to diagnose grazing rates and assess other loss terms [3,56]. Using seasonally biased data will accordingly impact quantification of carbon flux and net primary productivity for lower biomass areas.

Phytoplankton size is another area where accurate $b_{bp}(\lambda)$ observations are especially needed over the seasonal cycle. One particle size algorithm [6] uses $b_{bp}(\lambda)$ observations to track changes in particle size distributions from month to month. This algorithm has been used widely in ecological and carbon cycle studies. A recent carbon export study found that including particle size in ecological models improves the performance of those models [56], but an incorrect seasonal cycle of particle size will introduce bias into the modeled results. Introducing seasonal error into carbon cycle models may create a particularly significant issue for oligotrophic areas dominated by picophytoplankton, which have been getting more attention for their role in carbon export (see [57,58], and references therein). Oligotrophic regions may also be growing in areal extent due to climate change, and they are predicted to continue growing in future years [59], making them a substantial element of the global ocean system. If an artificial seasonality in phytoplankton size is introduced by algorithms built from ocean color $b_{bp}(\lambda)$, it will be difficult to predict the ecological fate of oligotrophic regions.

Our study has insufficiently characterized a seasonal bias in [chl] because we have only done so at the MOBY site using remote-sensing derivation, which represents a restricted range in

chlorophyll concentrations compared to the global distribution. Even so, we mention that any artificial seasonality in satellite chlorophyll may inadequately quantify phytoplankton physiology, growth rates, and phytoplankton community composition via empirically derived models for phytoplankton functional types [8,60,61].

D. Recommendations

Several additional top candidates (not explored here) for the source of the seasonal bias in $R_{rs}(\lambda)$, which are known to depend on angular geometry, include 1) instrument calibration; 2) atmospheric correction (other aspects beyond what is included here); 3) modeling of the water signal; and 4) system vicarious calibration. The instrument calibration could introduce a bias into $R_{rs}(\lambda)$ due to scan angle dependence, polarization corrections (which are a strong function of scattering angle), and other nonlinear effects, such as temperature dependencies. We note, however, that these characterizations can vary from instrument to instrument and may not offer a systematic reason for the observed bias across missions. Atmospheric correction estimates signals arising from molecular and aerosol scattering (as well as absorption) and it accounts for gaseous absorption (e.g., by ozone) and ocean surface effects (e.g., glint and whitecaps). Some of these effects are not well known or determined with sufficient accuracy, possibly yielding angular-dependent $R_{rs}(\lambda)$ errors. The retrieved signal from the water body, as viewed from space, needs to be corrected for diffuse atmospheric transmittance and normalized to yield $R_{rs}(\lambda)$ in a reference geometry. This requires proper modeling of bidirectional effects and interactions between the water body and the atmosphere. The current treatment might be improved by choosing a different BRDF (e.g., [62]), taking into account the water-leaving signal backscattered by the atmosphere, including anisotropy of the subsurface upwelling light field in the diffuse transmittance [63], and incorporating Earth sphericity [64,65]. The system vicarious calibration process aims to reduce the average temporal systematic bias for *in situ* and satellite observations at MOBY, but vicarious calibration does not address seasonal bias issues due to the instrument or the atmospheric correction [47]. For visible-band system vicarious calibration to be effective, the modeled atmospheric contributions need to be accurate and the near-infrared bands need to be adequately vicariously calibrated first [66]. Furthermore, vicarious calibration at MOBY is vulnerable to seasonal biases in match-up sample sizes because of Sun glint contamination at its latitude. An additional consideration is the Raman correction scheme applied to $R_{rs}(\lambda)$, because the effect of Raman scattering is greater at longer wavelengths and also scales with solar angle. The current Raman scattering correction schemes do not explicitly take solar angle into account, so revisiting Raman correction schemes may be merited.

We note that our multivariate regression analysis found that slopes of the Ångström coefficient and aerosol optical depth were more pronounced at mid-visible wavelengths, but less at shorter wavelengths. Typically, the choice of aerosol model, presented as the Ångström coefficient, affects shorter wavelengths more so than longer ones, due to the atmospheric correction assumptions of extrapolating the aerosol spectral dependence

from the near-infrared wavelengths. However, the slopes representing the BRDF were more pronounced at 412 and 443 nm than the aerosols' effect, suggesting a more complex underlying process that perhaps combine the effects of the BRDF and the aerosols correction, or more unknown parameters. The dynamic range of the ocean and the aerosol signals also play a role, since the dynamic range of the $R_{rs}(\lambda)$ can be orders of magnitude different from the blue end of the spectrum to the red end. Future work could explore different aerosol models and consider integrating CALIOP-derived aerosol optical depth information along with MODIS-Aqua data (as in [67], which showed substantial differences between CALIOP and MODIS-Aqua optical depth).

Until a solution to the seasonal bias is identified and implemented, we recommend additional consideration of CALIOP $b_{bp}(\lambda)$ data for global scale analyses when possible and prudent. Although the focus of this paper has been on the seasonal bias in ocean color $R_{rs}(\lambda)$, we have previously found annually averaged regional differences in estimated phytoplankton carbon from MODIS-Aqua compared to CALIOP of up to 50% [29], especially in low-biomass regions affected by the seasonal bias. For this reason, studies should acknowledge the seasonal bias when interpreting spatiotemporal patterns in ocean color data. Despite CALIOP's ~100 m footprint and the fact that it does not provide the comparable spatial coverage as SeaWiFS, MODIS-Aqua, and VIIRS, data from CALIOP can be averaged into the 1-deg monthly bins that are a common spatiotemporal resolution of models.

5. CONCLUSION

In this study, we provide evidence for global seasonal biases in satellite ocean color observations. Our findings can be summarized by the following points:

- The entire record of satellite ocean color over the last few decades is likely seasonally biased in low-biomass regions.
- Particulate backscattering from inversion models is most affected by a seasonal bias in $R_{rs}(\lambda)$, while phytoplankton and dissolved detrital absorption are less affected.
- The seasonal bias in $R_{rs}(\lambda)$ is most pronounced at longer wavelengths (i.e., > 531 nm) in a relative sense, noting that these signals are smaller in comparison with shorter wavelengths in open ocean water.
- Independent global observations are critical to validate remote-sensing products.
- Community efforts should help identify the root source of the problem, as all past, present, and future data (from the PACE mission, for example) will be affected until a solution can be implemented.

Supplemental document. See Supplement 1 for supporting content.

REFERENCES

1. M. J. Behrenfeld and P. G. Falkowski, "Photosynthetic rates derived from satellite-based chlorophyll concentration," Limnol. Oceanogr. **42**, 1–20 (1997).

2. T. Westberry, M. J. Behrenfeld, D. A. Siegel, and E. Boss, "Carbon-based primary productivity modeling with vertically resolved photoacclimation," Global Biogeochem. Cycles **22**, GB2024 (2008).

3. D. A. Siegel, K. O. Buesseler, S. C. Doney, S. F. Sailley, M. J. Behrenfeld, and P. W. Boyd, "Global assessment of ocean carbon export by combining satellite observations and food-web models," Global Biogeochem. Cycles **28**, 181–196 (2014).

4. D. Stramski, R. A. Reynolds, M. Kahru, and B. G. Mitchell, "Estimation of particulate organic carbon in the ocean from satellite remote sensing," Science **285**, 239–242 (1999).

5. H. Evers-King, V. Martinez-Vicente, R. J. Brewin, G. Dall'Olmo, A. E. Hickman, T. Jackson, T. S. Kostadinov, H. Krasemann, H. Loisel, R. Röttgers, S. Roy, D. Stramski, S. Thomalla, T. Platt, S. Sathyendranath, and S. Roy, "Validation and intercomparison of ocean color algorithms for estimating particulate organic carbon in the oceans," Front. Mar. Sci. **4**, 251 (2017).

6. T. S. Kostadinov, D. A. Siegel, and S. Maritorena, "Global variability of phytoplankton functional types from space: assessment via the particle size distribution," Biogeosciences **7**, 3239–3257 (2010).

7. H. Loisel, J. M. Nicolas, A. Sciandra, D. Stramski, and A. Poteau, "Spectral dependency of optical backscattering by marine particles from satellite remote sensing of the global ocean," J. Geophys. Res. Oceans **111**, C09024 (2006).

8. J. Uitz, H. Claustre, B. Gentili, and D. Stramski, "Phytoplankton class-specific primary production in the world's oceans: seasonal and interannual variability from satellite observations," Global Biogeochem. Cycles **24**, GB3016 (2010).

9. A. Bracher, M. Vountas, T. Dinter, J. P. Burrows, R. Röttgers, and I. Peeken, "Quantitative observation of cyanobacteria and diatoms from space using PhytoDOAS on SCIAMACHY data," Biogeosciences **6**, 751–764 (2009).

10. S. Sathyendranath, J. Aiken, and S. Alvain, " Phytoplankton functional types from Space," in Reports of the International Ocean-Colour Coordinating Group (IOCCG), Report Number 15 (International Ocean-Colour Coordinating Group, 2014), 156 pp.

11. S. J. Kramer, C. S. Roesler, and H. M. Sosik, "Bio-optical discrimination of diatoms from other phytoplankton in the surface ocean: evaluation and refinement of a model for the Northwest Atlantic," Remote Sens. Environ. **217**, 126–143 (2018).

12. P. K. Lange, P. J. Werdell, Z. Erickson, G. Dall'Olmo, R. J. W. Brewin, M. V. Zubkov, G. A. Tarran, H. A. Bouman, W. H. Slade, S. E. Craig, N. J. Poulton, A. Bracher, M. W. Lomas, and I. Cetinić, "Radiometric approach for the detection of picophytoplankton assemblages across oceanic fronts," Opt. Express **28**, 25682–25705 (2020).

13. H. Dierssen, G. B. McManus, A. Chlus, D. Qiu, B. C. Gao, and S. Lin, "Space station image captures a red tide ciliate bloom at high spectral and spatial resolution," Proc. Natl. Acad. Sci. USA **112**, 14783–14787 (2015).

14. G. Wei, D. Tang, and S. Wang, "Distribution of chlorophyll and harmful algal blooms (HABs): a review on space based studies in the coastal environments of Chinese marginal seas," Adv. Space Res. **41**, 12–19 (2008).

15. R. P. Stumpf, "Applications of satellite ocean color sensors for monitoring and predicting harmful algal blooms," Human Ecol. Risk Assess. Int. J. **7**, 1363–1368 (2001).

16. M. J. Behrenfeld, E. Boss, D. A. Siegel, and D. M. Shea, "Carbon-based ocean productivity and phytoplankton physiology from space," Global Biogeochem. Cycles **19**, GB1006 (2005).

17. M. J. Behrenfeld, T. K. Westberry, E. S. Boss, R. T. O'Malley, D. A. Siegel, J. D. Wiggert, B. A. Franz, C. R. McClain, G. C. Feldman, S. C. Doney, J. K. Moore, G. Dall'Olmo, A. J. Milligan, I. Lima, and N. Mahowald, "Satellite-detected fluorescence reveals global physiology of ocean phytoplankton," Biogeosciences **6**, 779–794 (2009).

18. T. K. Westberry and D. A. Siegel, "Spatial and temporal distribution of Trichodesmium blooms in the World's oceans," Global Biogeochem. Cycles **20**, GB4016 (2006).

19. R. P. Stumpf, "Sediment transport in Chesapeake Bay during floods: analysis using satellite and surface observations," J. Coastal Res. **4**, 1–15 (1988).

20. X. Yu, Z. Lee, F. Shen, M. Wang, J. Wei, L. Jiang, and Z. Shang, "An empirical algorithm to seamlessly retrieve the concentration of suspended particulate matter from water color across ocean to turbid river mouths," Remote Sens. Environ. **235**, 111491 (2019).

21. J. Tao and P. S. Hill, "Correlation of remotely sensed surface reflectance with forcing variables in six different estuaries," J. Geophys. Res. Oceans **124**, 9439–9461 (2019).

22. F. E. Hoge and P. E. Lyon, "Satellite observation of chromophoric dissolved organic matter (CDOM) variability in the wake of hurricanes and typhoons," Geophys. Res. Lett. **29**, 14–1–4 (2002).

23. A. Matsuoka, E. Boss, M. Babin, L. Karp-Boss, M. Hafez, A. Chekalyuk, C. W. Proctor, P. J. Werdell, and A. Bricaud, "Pan-Arctic optical characteristics of colored dissolved organic matter: tracing dissolved organic carbon in changing Arctic waters using satellite ocean color data," Remote Sens. Environ. **200**, 89–101 (2017).

24. S. Dutkiewicz, "Synergy between ocean colour and biogeochemical/ecosystem models," IOCCG Report Series No. 19 (International Ocean Colour Coordinating Group, 2020).

25. S. A. Henson, J. L. Sarmiento, J. P. Dunne, L. Bopp, I. Lima, S. C. Doney, J. John, and C. Beaulieu, "Detection of anthropogenic climate change in satellite records of ocean chlorophyll and productivity," Biogeosciences **7**, 621–640 (2010).

26. M. J. Behrenfeld, R. T. O'Malley, E. S. Boss, T. K. Westberry, J. R. Graff, K. H. Halsey, A. J. Milligan, D. A. Siegel, and M. B. Brown, "Revaluating ocean warming impacts on global phytoplankton," Nat. Climate Change **6**, 323–330 (2016).

27. S. Dutkiewicz, A. E. Hickman, O. Jahn, S. Henson, C. Beaulieu, and E. Monier, "Ocean colour signature of climate change," Nat. Commun. **10**, 578 (2019).

28. K. M. Bisson, E. Boss, T. K. Westberry, and M. J. Behrenfeld, "Evaluating satellite estimates of particulate backscatter in the global open ocean using autonomous profiling floats," Opt. Express **27**, 30191–30203 (2019).

29. K. M. Bisson, E. Boss, P. J. Werdell, A. Ibrahim, and M. J. Behrenfeld, "Particulate backscattering in the global ocean: a comparison of independent assessments," Geophys. Res. Lett. **48**, e2020GL090909 (2020).

30. N. Haëntjens, E. Boss, and L. D. Talley, "Revisiting ocean color algorithms for chlorophyll a and particulate organic carbon in the Southern Ocean using biogeochemical floats," J. Geophys. Res. Oceans **122**, 6583–6593 (2017).

31. E. Organelli, M. Barbieux, H. Claustre, C. Schmechtig, A. Poteau, A. Bricaud, E. Boss, N. Briggs, G. Dall'Olmo, F. D'Ortenzio, E. Leymarie, A. Mangin, G. Obolensky, C. Penkerc'h, L. Prieur, C. Roesler, R. Serra, J. Uitz, and X. Xing, "Two databases derived from BGC-Argo float measurements for marine biogeochemical and bio-optical applications," Earth Syst. Sci. Data **9**, 861–880 (2017).

32. C. D. Mobley, J. Werdell, B. Franz, Z. Ahmad, and S. Bailey, Atmospheric Correction for Satellite Ocean Color Radiometry (NASA Goddard Space Flight Center, Ocean Ecology Laboratory, 2016), https://oceancolor.gsfc.nasa.gov/docs/AtmosphericCorrection Tutorial.pdf.

33. Y. Xiong, X. Zhang, S. He, and D. J. Gray, "Re-examining the effect of particle phase functions on the remote-sensing reflectance," Appl. Opt. **56**, 6881–6888 (2017).

34. D. K. Clark, H. R. Gordon, K. J. Voss, Y. Ge, W. Broenkow, and C. Trees, "Validation of atmospheric correction over the oceans," J. Geophysical. Res. Atmos. **102**, 17209–17217 (1997).

35. P. J. Werdell, M. J. Behrenfeld, P. S. Bontempi, E. Boss, B. Cairns, G. T. Davis, B. A. Franz, U. B. Gliese, E. T. Gorman, O. Hasekamp, K. D. Knobelspiesse, A. Mannino, J. V. Martins, C. R. McClain, G. Meister, and L. A. Remer, "The plankton, aerosol, cloud, ocean Ecosystem mission: status, science, advances," Bull. Am. Meteorol. Soc. **100**, 1775–1794 (2019).

36. G. C. Feldman, "SeaBass file search," NASA, accessed 2021, https://seabass.gsfc.nasa.gov/search.

37. S. W. Bailey and P. J. Werdell, "A multi-sensor approach for the on-orbit validation of ocean color satellite data products," Remote Sens. Environ. **102**, 12–23 (2006).

38. B. N. Seegers, R. P. Stumpf, B. A. Schaeffer, K. A. Loftin, and P. J. Werdell, "Performance metrics for the assessment of satellite data products: an ocean color case study," Opt. Express **26**, 7404–7422 (2018).

39. https://oceancolor.gsfc.nasa.gov/atbd/chlor_a.

40. P. J. Werdell, B. A. Franz, S. W. Bailey, G. C. Feldman, E. Boss, V. E. Brando, M. Dowell, T. Hirata, S. J. Lavender, Z. Lee, H. Loisel, S. Maritorena, F. Mélin, T. S. Moore, T. J. Smyth, D. Antoine, E. Devred, O. H. F. d'Andon, and A. Mangin, "Generalized ocean color inversion model for retrieving marine inherent optical properties," Appl. Opt. **52**, 2019–2037 (2013).

41. G. C. Feldman, "SeaBASS regional time series tool," NASA, accessed 2021, https://seabass.gsfc.nasa.gov/timeseries/.

42. M. J. Behrenfeld, Y. Hu, C. A. Hostetler, G. Dall'Olmo, S. D. Rodier, J. W. Hair, and C. R. Trepte, "Space-based lidar measurements of global ocean carbon stocks," Geophys. Res. Lett. **40**, 4355–4360 (2013).

43. M. J. Behrenfeld, P. Gaube, A. Penna, R. T. O'Malley, W. J. Burt, Y. Hu, P. S. Bontempi, D. K. Steinberg, E. S. Boss, D. A. Siegel, C. A. Hostetler, P. D. Tortell, and S. C. Doney, "Lidar: monthly MAT files from CALIOP data," Ocean Productivity, accessed 2021, http://orca.science.oregonstate.edu/lidar_nature_2019.php.

44. X. Lu, Y. Hu, Y. Yang, P. Bontempi, A. Omar, and R. Baize, "Antarctic spring ice-edge blooms observed from space by ICESat-2," Remote Sens. Environ. **245**, 111827 (2020).

45. L. Lacour, R. Larouche, and M. Babin, "In situ evaluation of space-borne CALIOP lidar measurements of the upper-ocean particle backscattering coefficient," Opt. Express **28**, 26989–26999 (2020).

46. J. Salvatier, T. V. Wiecki, and C. Fonnesbeck, "Probabilistic programming in Python using PyMC3," PeerJ Comput. Sci. **2**, e55 (2016).

47. B. A. Franz, S. W. Bailey, P. J. Werdell, and C. R. McClain, "Sensor-independent approach to the vicarious calibration of satellite ocean color radiometry," Appl. Opt. **46**, 5068–5082 (2007).

48. D. K. Clark, M. A. Yarbrough, M. Feinholz, S. Flora, W. Broenkow, Y. S. Kim, B. C. Johnson, S. W. Brown, M. Yuen, and J. L. Mueller, "Chapter 2: MOBY, a radiometric buoy for performance monitoring and vicarious calibration of satellite ocean color sensors: measurement and data analysis protocols," in Ocean Optics Protocols for Satellite Ocean Color Sensor Validation. Revision 4 (NASA, Goddard Space Flight Center, 2003).

49. M. J. Behrenfeld, S. C. Doney, I. Lima, E. S. Boss, and D. A. Siegel, "Annual cycles of ecological disturbance and recovery underlying the subarctic Atlantic spring plankton bloom," Global Biogeochem. Cycles **27**, 526–540 (2013).

50. D. A. Siegel, S. C. Doney, and J. A. Yoder, "The North Atlantic spring phytoplankton bloom and Sverdrup's critical depth hypothesis," Science **296**, 730–733 (2002).

51. C. A. Hostetler, M. J. Behrenfeld, Y. Hu, J. W. Hair, and J. A. Schulien, "Spaceborne lidar in the study of marine systems," Annu. Rev. Mar. Sci. **10**, 121–147 (2018).

52. S. W. Brown, S. J. Flora, M. E. Feinholz, M. A. Yarbrough, T. Houlihan, D. Peters, Y. S. Kim, J. L. Mueller, B. C. Johnson, and D. K. Clark, "The marine optical buoy (MOBY) radiometric calibration and uncertainty budget for ocean color satellite sensor vicarious calibration," Proc. SPIE **6744**, 67441M (2007).

53. L. Li, D. Stramski, and R. A. Reynolds, "Effects of inelastic radiative processes on the determination of water-leaving spectral radiance from extrapolation of underwater near-surface measurements," Appl. Opt. **55**, 7050–7067 (2016).

54. E. Boss, N. Haëntjens, S. G. Ackleson, B. Balch, A. Chase, G. Dall'Olmo, S. Freeman, Y. Liu, J. Loftin, W. Neary, N. Nelson, M. Novak, W. Slade, C. Proctor, P. Tortell, and T. Westberry, IOCCG Ocean Optics and Biogeochemistry Protocols for Satellite Ocean Colour Sensor Validation, Inherent Optical Property Measurements and Protocols: Best Practices for the Collection and Processing of Ship-Based Underway Flow-Through Optical Data (v4. 0), OCCG Protocol Series 2019-11 (IOCCG, 2019).

55. J. R. Graff, T. K. Westberry, A. J. Milligan, M. B. Brown, G. Dall'Olmo, V. van Dongen, K. M. Reifel, and M. J. Behrenfeld, "Analytical phytoplankton carbon measurements spanning diverse ecosystems," Deep Sea Res. I **102**, 16–25 (2015).

56. K. Bisson, D. A. Siegel, and T. DeVries, "Diagnosing mechanisms of ocean carbon export in a satellite-based food web model," Front. Mar. Sci. **7**, 505 (2020).

57. T. L. Richardson and G. A. Jackson, "Small phytoplankton and carbon export from the surface ocean," Science **315**, 838–840 (2007).

58. T. L. Richardson, "Mechanisms and pathways of small-phytoplankton export from the surface ocean," Annu. Rev. Mar. Sci. **11**, 57–74 (2019).

59. A. J. Irwin and M. J. Oliver, "Are ocean deserts getting larger?" Geophys. Res. Lett. **36**, L18609 (2009).

60. T. Hirata, N. J. Hardman-Mountford, R. J. W. Brewin, J. Aiken, R. Barlow, K. Suzuki, T. Isada, E. Howell, T. Hashioka, M. Noguchi-Aita, and Y. Yamanaka, "Synoptic relationships between surface Chlorophyll-a and diagnostic pigments specific to phytoplankton functional types," Biogeosciences **8**, 311–327 (2011).

61. M. A. Soppa, T. Hirata, B. Silva, T. Dinter, I. Peeken, S. Wiegmann, and A. Bracher, "Global retrieval of diatom abundance based on phytoplankton pigments and satellite data," Remote Sens. **6**, 10089–10106 (2014).

62. Y. J. Park and K. Ruddick, "Model of remote-sensing reflectance including bidirectional effects for case 1 and case 2 waters," Appl. Opt. **44**, 1236–1249 (2005).

63. H. Yang and H. R. Gordon, "Remote sensing of ocean color: assessment of water-leaving radiance bidirectional effects on atmospheric diffuse transmittance," Appl. Opt. **36**, 7887–7897 (1997).

64. R. J. Frouin, B. A. Franz, A. Ibrahim, K. Knobelspiesse, Z. Ahmad, B. Cairns, J. Chowdhary, H. M. Dierssen, J. Tan, O. Dubovik, X. Huang, A. B. Davis, O. Kalashnikova, D. R. Thompson, L. A. Remer, E. Boss, O. Coddington, P.-Y. Deschamps, B.-C. Gao, L. Gross, O. Hasekamp, A. Omar, B. Pelletier, D. Ramon, F. Steinmetz, and P.-W. Zhai, "Atmospheric correction of satellite ocean-color imagery during the PACE era," Front. Earth Sci. **7**, 145 (2019).

65. D. Ramon, F. Steinmetz, D. Jolivet, M. Compiègne, and R. Frouin, "Modeling polarized radiative transfer in the ocean-atmosphere system with the GPU-accelerated SMART-G Monte Carlo code," J. Quant. Spectrosc. Radiat. Transfer **222**, 89–107 (2019).

66. B. B. Barnes, C. Hu, S. W. Bailey, and B. A. Franz, "Sensitivity of satellite ocean color data to system vicarious calibration of the long near infrared band," IEEE Trans. Geosci. Remote Sens. **59**, 2562–2578 (2020).

67. M. H. Kim, S. W. Kim, S. C. Yoon, and A. H. Omar, "Comparison of aerosol optical depth between CALIOP and MODIS-Aqua for CALIOP aerosol subtypes over the ocean," J. Geophys. Res. Atmos. **118**, 13–241 (2013).

68. G. C. Feldman, "OceanColor Web," NASA, accessed 2021, https://oceancolor.gsfc.nasa.gov.

69. Argo, "Argo DAC," Argo/Global Ocean Observing System, accessed 2021, http://www.argodatamgt.org/Access-to-data.